Chemical Geology 695 (2025) 123068

Contents lists available at ScienceDirect

Chemical Geology

journal homepage: www.elsevier.com/locate/chemgeo

Research Paper

Elemental signatures of metamorphic, diagenetic, and pedogenic magnesites from Central Queensland, Australia

Carl Swindle [a,d,*], Paulo Vasconcelos [b], Zoe Dimarco [b], Nathan Dalleska [a], Ai Nguyen [b], Emily Cardarelli [c,e], Surjyendu Bhattacharjee [a], Kenneth Farley [a], Theodore Present [a]

[a] *Division of Geological and Planetary Sciences, California Institute of Technology, Pasadena, CA 91125, United States of America*
[b] *School of the Environment, The University of Queensland, Brisbane, Queensland 4072, Australia*
[c] *NASA Jet Propulsion Laboratory, California Institute of Technology, Pasadena, CA 91109, United States of America*
[d] *The B. John Garrick Institute for the Risk Sciences, University of California, Los Angeles, Los Angeles, CA 90095, United States of America*
[e] *Department of Earth, Planetary and Space Sciences, University of California, Los Angeles, Los Angeles, CA 90095, United States of America*

ARTICLE INFO

Editor: Vasileios Mavromatis

Keywords:
Magnesite
Rare earth elements
Jezero Crater analog
Paleoenvironment

ABSTRACT

Magnesium carbonates record information on water-rock interactions during and after mineral precipitation. The Marlborough Terrane in central Queensland, Australia, contains magnesite-bearing serpentinite highlands surrounded by low-lying sedimentary basins that host authigenic magnesite ($MgCO_3$). Open pit mines in both settings provide exposures of serpentinites (Gumigil) and Cenozoic sediments and overlying black soils (Yaamba) that host the magnesite and other authigenic phases. The Gumigil mine contains deeply weathered serpentinite hosting metamorphic magnesite veins that formed *syn*-tectonically; both serpentinite and magnesite are now partially dissolving, silicifying, and ferruginizing. Aqueous Mg^{2+} is being exported into the basins surrounding the serpentinite ridges. The Yaamba magnesite mine in the surrounding plains exposes diagenetic magnesite formation within unlithified alluvial sediments, where ascending magnesium-rich groundwaters replace arkosic sands and silts by magnesite cements, nodules, and pinnacles. Late-stage pedogenic processes at Gumigil and Yaamba drive retrograde transformation of magnesite into geochemically distinct exterior regions of second-generation cryptocrystalline magnesite recording interactions with Fe/Mn-oxides/hydroxides via cerium anomalies, yttrium anomalies and manganese concentrations in zoned magnesites from Yaamba. The complex history of mineral precipitation, dissolution, diagenetic replacement, and supergene alteration is recorded in the major, minor and trace element compositions of magnesites at each site. Serpentinite ridges and magnesite-bearing valley floors in Central Queensland provide a useful analog to the processes that might occur in the ultramafic highlands and carbonated lowlands at Jezero crater, Mars.

1. Introduction

The chemical composition of Mg-carbonates in Martian meteorites or in samples collected on the surface of Jezero Crater may place constraints on the water and carbon cycles on Mars billions of years ago (Borg et al., 1999; Eiler et al., 2002; Farley et al., 2022; Liu et al., 2022; Scheller et al., 2022). In particular, carbonates in Martian meteorite ALH84001 and outcrops recently discovered by the Mars 2020 Perseverance Rover in Jezero Crater may have formed during low-temperature, near-surface aqueous alteration of ultramafic protoliths and surrounding sedimentary deposits, from hydrothermal alteration, or from Mg-rich fluids derived from the weathering of ultramafic rock (Eiler et al., 2002; Farley et al., 2022; Halevy et al., 2011; Scheller et al., 2022; Stack et al., 2024; Sun et al., 2023). Their elemental compositions, determined in meteorites or after sample-return, will help to unravel dominant aqueous conditions during magnesite precipitation.

On Earth, carbonates forming from groundwater or soil waters tend to be calcitic or dolomitic (Alonso-Zarza and Wright, 2010b; Alonso-Zarza and Wright, 2010a), forming soil nodules or indurated horizons called palustrine carbonates or calcretes. Terrestrial calcium carbonates and the processes by which their elemental compositions record paleoenvironmental information on Earth are studied extensively (Elderfield et al., 2010; Lachniet, 2009; Srivastava et al., 2019; Vaniman and Whelan, 1994; Zhang and Shields, 2022). The greater crustal abundance

---

* Corresponding author at: Division of Geological and Planetary Sciences, California Institute of Technology, Pasadena, CA 91125, United States of America.
E-mail address: cswindle@ricksciences.ucla.edu (C. Swindle).

https://doi.org/10.1016/j.chemgeo.2025.123068
Received 21 August 2025; Received in revised form 19 September 2025; Accepted 20 September 2025

of Ca on Earth's surface compared to Mars produces few terrestrial examples of Mg-rich carbonates relative to Ca-carbonates (Scheller et al., 2021). On Earth, Mg-rich carbonates form in a variety of settings, but are often associated with serpentinites, and form over a wide range of temperatures (e.g., Gahlan et al., 2020; Kelemen and Matter, 2008; Mervine et al., 2014; Rielli et al., 2022; Russell et al., 1999; Ternieten et al., 2021). Most surface forming Mg-rich carbonates are hydrous minerals in palustrine and lacustrine settings such as Lake Salda in Turkey, the Cariboo Plateau and the Atlin Playa System in Canada, springs from Samail Ophiolite springs in Oman and in the Ronda peridotites in Spain, and the Coorong Lakes in Australia (Giampouras et al., 2019, 2020; Power et al., 2009; Raudsepp et al., 2024; Russell et al., 1999; Warren, 1990). Therefore, anhydrous magnesium carbonates forming from groundwaters in sedimentary rocks are less studied (Scheller et al., 2021), with a few exceptions (e.g., De Deckker, 2019; Kaya et al., 2023; Oskierski et al., 2013a), especially for fluvial-deltaic sediments similar to those observed in Jezero Crater and Gale Crater (Caravaca et al., 2024; Stack et al., 2024; Tutolo et al., 2025). Geochemical signatures preserved in similar Mg-carbonates on Mars could shed light on near-surface paleoenvironmental conditions of ancient Mars. Thus, assessment of elemental behavior during Mg-carbonate precipitation and alteration on Earth may assist with interpretation of Martian rocks rich in these minerals such as those sampled by *Perseverance* for eventual return to Earth. Particularly, the capacity for trace elements in magnesite to capture and preserve signatures that record 1) hydrological conditions (e.g., Eh-pH) and 2) fluid provenance has yet to be assessed in fluvial sedimentary environments from source to sink.

To address this knowledge gap, we sampled and analyzed magnesites from two related sites in central Queensland, Australia (Fig. 1): magnesite veins in weathered serpentinites at the ridge-top Gumigil Mine; and diagenetic magnesite concretions, nodules, and pinnacles that replace arkosic sands in the surrounding alluvial plains (Yaamba Mine). Open pit mining exposures capture distinct stages of the Mg-cycle from source to sink, including (1) metamorphic formation of magnesite veins, (2) weathering of magnesite veins and host serpentinites, (3) Mg^{2+} leaching during chemical weathering and erosion from ultramafic source rocks, (4) aqueous Mg^{2+} migration in groundwaters, and (5) both diagenetic and pedogenic magnesite precipitation in alluvial sediments and black soil plains. In addition, this work utilizes μXRF mapping techniques to identify and target chemically distinct zones (invisible to the naked eye) in individual magnesite nodules and veins to avoid mixing away geochemical heterogeneity critical for tracking paleoenvironmental processes. Results demonstrate that these magnesite samples can capture and preserve hydrological trace element signatures in a Jezero Crater analog environment on Earth.

2. Geologic background

In central Queensland, the Upper Devonian to Triassic New England Orogeny emplaced the Princhester Serpentinite adjacent to Paleozoic sedimentary and volcanic units of the Marlborough block (Jessop et al., 2019; Murray, 2007) (Fig. 1). These units were intruded by syn-orogenic magmatic suites, primarily of granite and granodiorite compositions (Murray, 2007; Murray et al., 1997). Following the orogeny, during low-grade metamorphism and hydrothermal alteration of ultramafic rocks, erosion and fluvial sedimentation produced low-lying basins surrounded by up to 400 m residual plateaus and ridges that remained exposed to long-term weathering (Croke et al., 2011; Milburn and Wilcock, 1994, 1998; Wilcock, 2000). Lateritic weathering of serpentinites leached aqueous Mg^{2+} ions into groundwaters that were transported into low-lying areas, where they combined with aqueous carbonate species to form magnesite nodules, concretions, and pinnacles in alluvial sediments (Eggleton et al., 2011; Foster and Eggleton, 2002; Milburn and Wilcock, 1994, 1998; Searston, 1998; Wilcock, 2000).

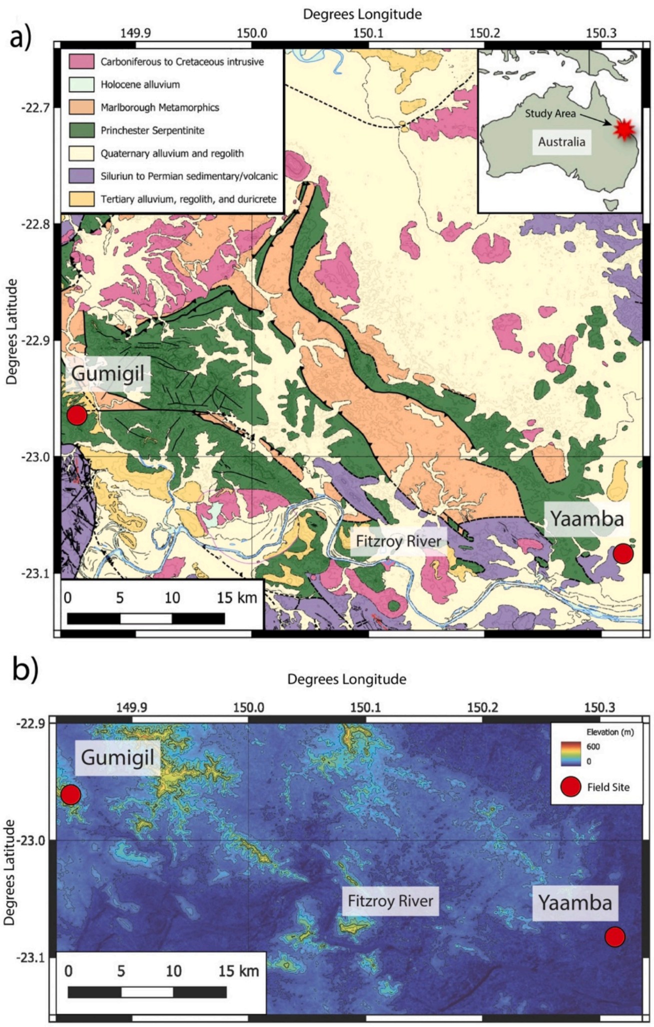

Fig. 1. Geologic and elevation maps of the study area. Panel (a) is geologic map contextualizing the Gumigil and Yaamba Mines (red dots) along with the Fitzroy River (opaque blue), which flows eastward. This map contains data provided by the State of Queensland Department of Natural Resources and Mines (2012). The upper sub-panel in panel (a) shows the study area in context with the continent of Australia. Panel (b) is an elevation map showing the two mines with topographic context. Country boundary data was made with Natural Earth. Free vector and raster map data is available at naturalearthdata.com. Elevation data was sourced from the Aster GDEM v3 (Abrams et al., 2022). (For interpretation of the references to colour in this figure legend, the reader is referred to the web version of this article.)

2.1. *Gumigil chrysoprase mine: weathered Princhester Serpentinite*

The Princhester Serpentinite formed by metasomatic hydrothermal alteration of Neoproterozoic or early Cambrian peridotitic harzburgites and pyroxenites (Bruce et al., 2000; Murray, 2007) (Fig. 1). It is now structurally intercalated with metasediments and interpreted as a section of oceanic lithospheric mantle obducted into a forearc accretionary wedge complex during the New England Orogeny (Murray, 2007). The Princhester Serpentinite hosts folded and faulted magnesite vein structures that predate exhumation (Eggleton et al., 2011). After exhumation in the Cenozoic, the serpentinite protolith underwent prolonged erosion and weathering, resulting in laterization and formation of residual silcretes and ferricretes that now cap weathered ultramafic plateaus and ridges at 250–380 m-elevation (Eggleton et al., 2011; Foster and Eggleton, 2002) or deeply dissected weathered hills at 50–70 m elevation (Fig. 2). During weathering, many veins were replaced by cryptocrystalline and amorphous silica that often contains nickeliferous

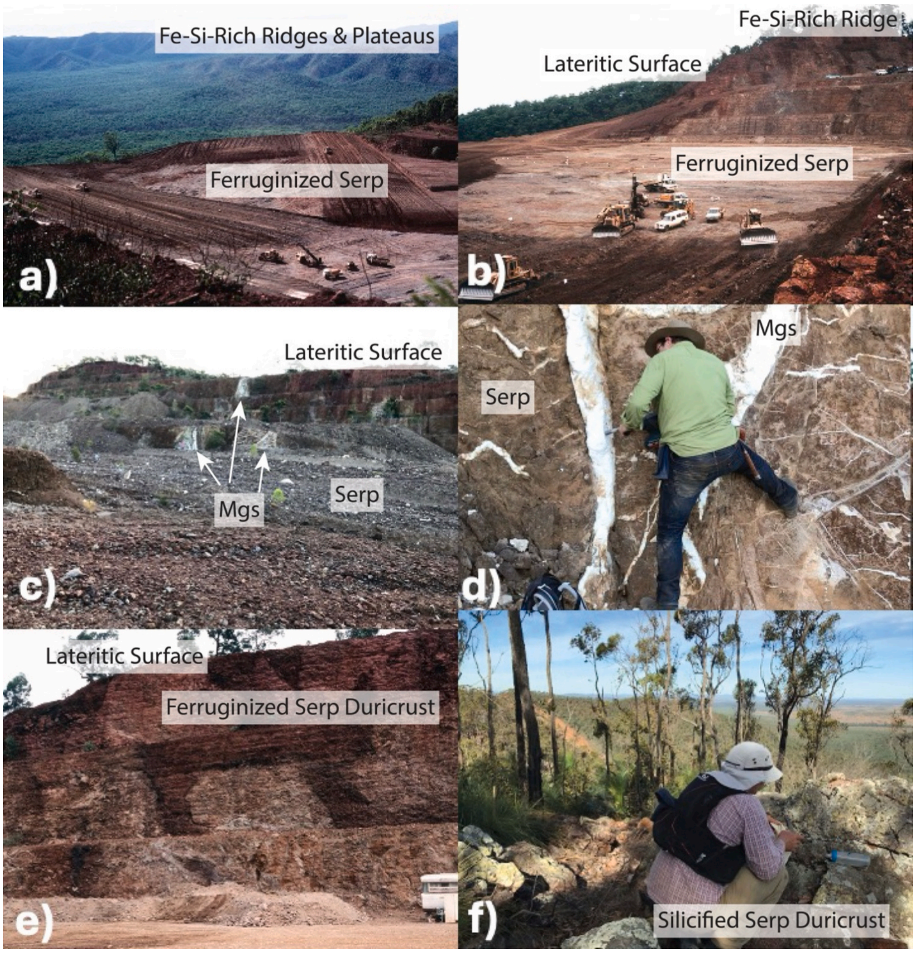

Fig. 2. Photographs at the Gumigil Mine field site. In the Marlborough-Kunwarara region of Central Queensland, (a) serpentinite iron and silica-rich ridges and plateaus where lateritic weathering profiles host (b) chrysoprase deposits, such as the open pit Gumigil mine. Panels b-d show lateritic profiles transitioning into weathered and then pristine serpentinites (Serp) at depth: sequentially from the lateritic surface (b), intermediate sections of the pit (c), and deeper in the pit where serpentinite outcrops with magnesite (Mgs) veins are exposed (d). The serpentinites host erratically distributed folded and faulted magnesite veins, suggesting that serpentinite-hosted magnesite veins formed during the alteration of peridotites into serpentinites before or during the emplacement of the serpentinite bodies. Panels e and f illustrate the elevated residual landscapes, where strongly ferruginized-silicified serpentinite blocks devoid of Mg indicate large-scale transport of Mg from ridge tops to the surrounding plains.

layered silicates; this supergene material, called chrysoprase, is the target of the mining operation. A high-elevation (350–370 m) ridge hosts the Gumigil chrysoprase mine (Fig. 1), which exposes a deep lateritic weathering profile (Eggleton et al., 2011; Foster and Eggleton, 2002; Murray, 2007).

2.2. *Yaamba magnesite mine: diagenetic and pedogenic magnesites*

The Yaamba magnesite mine (Fig. 1) sits at ~20 m elevation within the Fitzroy River catchment ~6 km north of the modern Fitzroy River and ~ 45 km from the Gumigil mine. The Yaamba pit is within 5 km of the Princhester serpentinite ridges and plateaus and within 5 km from the ~60 m elevation Brolga Ni—Co laterite mine; serpentinites probably constitute a substantial portion of the Yaamba pit bedrock along with magmatically-differentiated igneous and sedimentary crustal units (Murray et al., 1997). In the 1980's, the Yaamba magnesite deposit was estimated to cover ~27 km^2 and host ~188 million tons of raw magnesite within ~460 million tons of sediment (Matheson, 1988). Sedimentary units hosting magnesite were likely deposited during the Cenozoic and as recently as the Quaternary (Croke et al., 2011; Jessop et al., 2019; Murray et al., 1997; Pope, 2007).

3. Methods

3.1. *Sampling and selective analysis*

Vein magnesites and their host serpentinites were collected in outcrops exposed at mine walls and floors at the Gumigil mine (Figs. 2 and 3). Nodular magnesites were sampled at Yaamba together with co-existing sediments and Fe/Mn-oxides pisolith from overlying soils (Figs. 4 and 5). Sample names, locations, and type (rock, vein, concretion, sediment, or pisolith) are summarized in Table S1. Since slabs of magnesite nodules and veins typically appear homogenous and white, microscale X-ray fluorescence (μXRF) mapping was used to produce chemical images of the polished slabs of magnesite nodules, which guided further subsampling by drilling powders using a high-speed rotary drill.

3.2. *Micro-XRF mapping*

Chemical imaging of a subset (M22–028, M22–029, M22–214, M22–216, M22–220, M22–311, M22–312, and M22–313) of slabbed samples was accomplished with a Bruker M4 Tornado benchtop μXRF spectrometer in the Caltech Division of Geological and Planetary Science Analytical Facility (Fig. 5). X-rays were generated from a rhodium tube

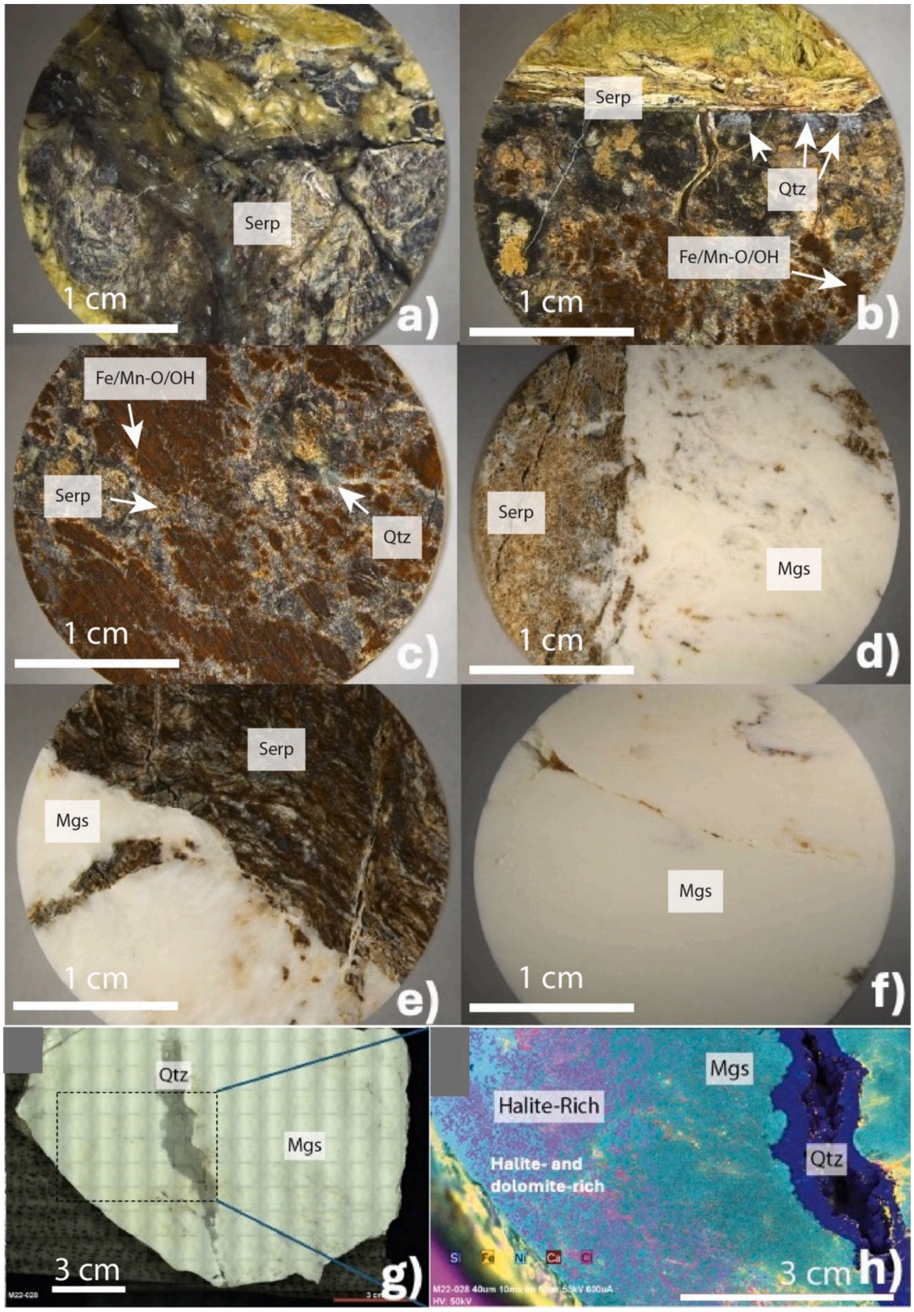

Fig. 3. One-inch drill-cores (a-f) of serpentinites and magnesites and a slab with a supergene quartz vein crosscutting a magnesite vein (g-h) from Gumigil (a) serpentinite; (b) partially weathered and silicified serpentinite; (c) strongly weathered and silicified serpentinite; (d-e) partially weathered serpentinite contact with metamorphic magnesite vein; (f) metamorphic magnesite vein; (g-h) partially silicified metamorphic magnesite with supergene pore-filling halite and dolomite. Panel h is a subsection of panel g. The Fe/Mn-O/OH label represents Fe/Mn-oxides/hydroxides.

excited to 50 kV with 600 μA current and were focused onto samples with polycapillary optics as samples were rastered beneath the primary X-ray beam. Analyses were performed under vacuum (ca. 2 mbar) to maximize sensitivity to magnesium and other light elements. Fluorescent X-ray energy spectra were measured simultaneously on two 30 mm^2 silicon drift energy dispersive spectrometer detectors and assigned to 40 μm-wide pixels, which had primary beam dwell times of 5 to 10 ms per pixel. Bruker software (Bruker M4 Tornado v. 1.6) was used to deconvolve fluorescent X-ray EDS spectra from background, emission line overlaps, and detector artifacts (i.e., pile-up peaks and detector escape peaks).

A slab of nodular magnesite (sample M22–308) underwent analysis by the modified iXRF Atlas X instrument at the Centre of Microscopy and Microanalysis (CMM), at theUniversity of Queensland. Micro-XRF elemental mapping was conducted at 50 kV (1000 μA) using a molybdenum-target tube with polycapillary focusing optics producing 17.4 keV X-rays (flux of 2.2×108 pH.s^{-1}) focusing to 25 μm. The Mo-source was defocused to 80 μm for mapping of sample M22–308. Following acquisition, data was processed and visualized in GeoPIXE version 8.7 (CSIRO) (Ryan, 2001; Ryan et al., 2015) using the UQ facility's in-house dynamic analysis (DA) model. A uniform sample composition ($MgCO_3$) was assumed for the fluorescent yield calculation.

3.3. Whole rock analyses

Magnesite and serpentinite samples were cored using a diamond

Fig. 4. The Yaamba Mine profile consists, from the surface downward, of a relatively thin black soil profile overlying a magnesite-rich sand layer (a-b). Sands have both horizontal laminar beds and cross bedded sections (c-d). Magnesites in the sands (e-f) becomes purer and more abundant with depth.

rotary drill in the Sample Preparation Laboratory at the University of Queensland (Fig. 3a-f). In magnesite samples, coring was exclusively conducted in zones where non-carbonate inclusions were visually absent. In addition, 10 g (g) of one Yaamba sediment sample was oven-dried at 30 °C for multiple days to remove water. Samples were subsequently crushed using a hydraulic press, followed by a percussion hammer to comminute grains to sub-2 mm grains. Crushed samples were pulverized to 17 μm grain-size powders using an agate ball mill; milling lasted from 7 to 15 min, depending on the nature of the sample. Sample contamination was minimized by thoroughly cleaning crushing equipment between each sample. The cleaning procedure involved pulverizing clean sand in the agate ball mill between each sample to lower the risk of sample cross contamination.

Further sample preparation was conducted for Loss on Drying (LOD), Loss On Ignition (LOI), major, minor and trace element analyses at the Environmental Geochemistry Laboratory (EGL) at the University of Queensland. An aliquot of ~2.5 g from each sample was weighed, oven-dried at 105 °C for 1 h, and re-weighed to determine LOD. The dried sample was then further heated in a muffle furnace at 1000 °C for one hour to obtain LOI.

The major element (oxide) composition was obtained through alkaline fusion followed by the analysis. Approximate 0.1 g of each sample was mixed with 0.6 g of lithium borate in a platinum crucible and was fused by steps up to 1000 °C. The resulting glass bead was cast into 100 mL 5 % HNO_3 and analyzed using a Perkin Elmer Optima 8300 DV ICP-OES.

Minor and trace elements were analyzed from acid digests using an Agilent 7900 ICP-MS. Prior to digestion, approximate 1 g of each Yaamba sample was ashed at 500 °C to remove any organic matter that would complicate the digestion process. The weight loss of each sample was carefully recorded for later calculation.

Approximately 0.1 g of each magnesite, serpentinite, and ashed Yaamba sediment sample was weighed and first digested with 2 mL of concentrated HNO_3 and 0.5 mL H_2O_2 in sealed Teflon digestive beakers on a hot plate 140 °C overnight to remove carbonate component. The resulting solution was evaporated down to incipient dryness at 80–90 °C. The dried residue was then digested with a mixture of 1 mL of concentrated HNO_3 and 3 mL of concentrated HF on a hotplate at 140 °C. This step was used to ensure silica-bearing minerals in the samples are completely dissolved. The digest solution was then evaporated at again at 80–90 °C before re-dissolving with 2 % HNO_3 and diluted further to 4000× for minor and trace element analysis.

3.4. Selective digestion and major and trace element determination in magnesite

Despite their mineralogical homogeneity, the magnesite nodules may contain small amounts of acid-soluble sediment, soil, and protolith phases such as oxide or clay minerals. To minimize their contribution during digestion of the carbonate minerals, samples were pre-cleaned

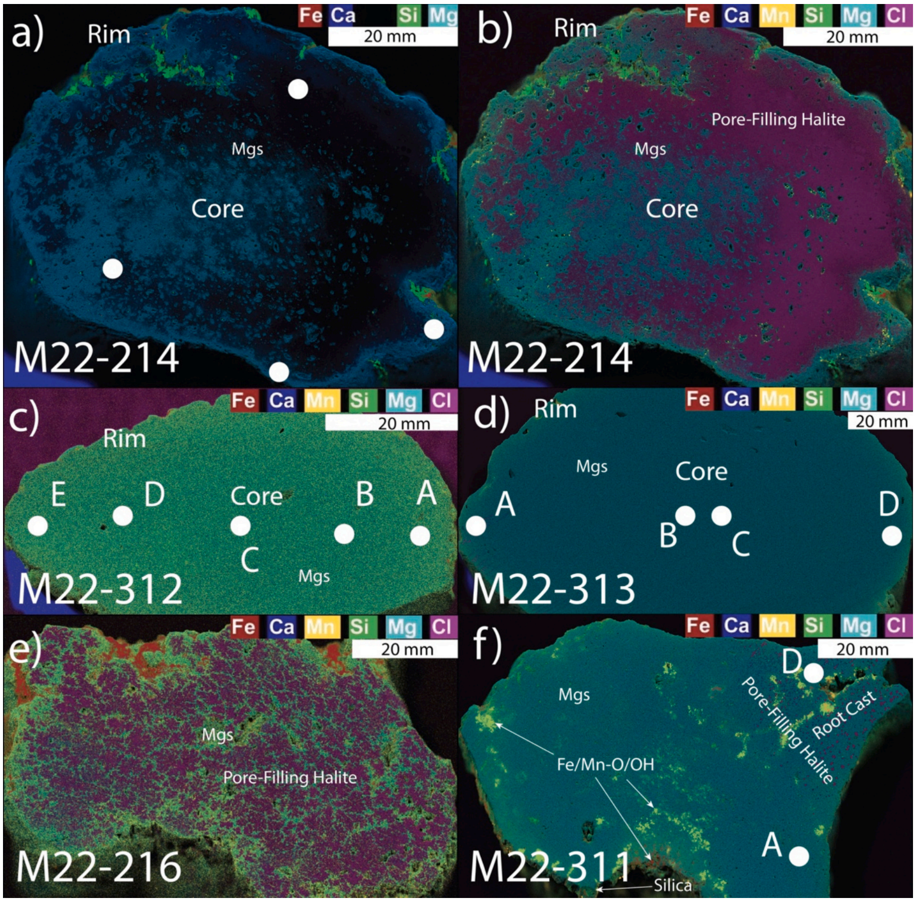

Fig. 5. μXRF images of slabbed magnesite nodules from Yaamba showing elemental distributions. (a-b) M22–214 nodule showing some remnant quartz grains and NaCl filling magnesite pores; (c) M22–312 homogeneous clean nodule; (d) M22–313 clean nodule with Mn-rich rim; (e) M22–216 heterogeneous contaminated nodule with remnant sand and large amount of dendritic NaCl precipitation; (f) M22–311 strongly contaminated nodule with irregularly distributed Mn-oxides, Fe-oxides, and NaCl.

and gently digested following protocols developed for calcium carbonate minerals (Cao et al., 2020; Swindle et al., 2025; Swindle, 2023). Powder (4.5–9.0 mg) was extracted from visually pure sections of magnesite using a diamond-studded high-speed rotary drill (Dremel). Powder extraction was preceded by pre-abrasion of the sampling area to remove surficial contaminants. To remove water-soluble salts and cations adsorbed to the surfaces of mineral grains, powders were ultrasonicated with two rinses in neutral ammonium acetate solution and three rinses in ultrapure water (Milli-Q). Powders were subsequently digested in 0.3 M acetic acid at 90 °C, passed through 0.2-μm syringe filters to remove insoluble silicates and metal-oxides/hydroxides and brought up in 5 % nitric acid prior to analysis on an Agilent 8800 ICP-MS at Caltech. For quality control, we used the DWA-1 dolomite sourced from Brammer Standard. Elements were measured within the reported uncertainties of the DWA-1 reference values (Roelandts and Duchesne, 1994). Standards were matrix matched with Mg^{2+} and Ca^{2+} when DWA-1 dolomite was analyzed (there is no adequate reference standard for magnesite). Trace element concentrations were determined by normalizing elements to the Mg^{2+} and Ca^{2+} concentrations in solution (>99 % of the cations) with the calculated carbonate content needed for stoichiometric $MgCO_3$ and $CaCO_3$. Elements such as Si, Al, P, and many others were monitored in quick scan mode. Large shifts in analyte data would have resulted in a rejection due to contamination.

4. Results

4.1. Field, mineralogy, and textural observations

4.1.1. Gumigil chrysoprase mine

Magnesite veins in the Gumigil mine are common in fault-bound serpentinite blocks that range from shallow depths to several 10's of meters beneath the current surface (Fig. 2). At depth, magnesites are milky white, cryptocrystalline, pure, porous, and have an elongated granular texture with apparent internal folding (Figs. 2 and 3). Magnesite veins observed are millimeters to tens of centimeters wide and occur as complex fracture networks in serpentinite (Figs. 2 and 3).

Towards the surface, magnesite veins become partially or completely replaced by supergene silica (quartz, chalcedony, opal, and chrysoprase, and prase opal) veins. Vein margins are more porous and often have a bulbous cauliflower texture attributed to weathering of isotropic, fine-grained material. Pore-filling halite and minor dolomite occur in recrystallized margins of some magnesite veins (Fig. 3h).

4.1.2. Yaamba magnesite mine

Open mining pits at Yaamba expose ~9 m of unlithified cross bedded and laminated arkosic to sub-arkosic sands, silts, and clayey silts locally cemented and partially or completely replaced by magnesite nodules, concretions, and pinnacles (Fig. 4). The sediments at Yaamba were deposited in a sand-rich river system with largescale barforms like the modern Fitzroy River and are now part of a terraced flood plain with more extensive soil development. The sand is mostly detrital quartz and feldspars sourced from regional granitoid and metamorphic rocks, with sparse chromite derived from ultramafic rocks. Trough cross beds up to 40 cm thick form channel deposit bedsets that are several meters thick and 10 to 50 m wide (Fig. 4). Some clay in flaser bedded silt in the uppermost 3 m of the pit could be depositional, but grain shapes, sizes, and textures suggest that most clays are authigenic and grew along trough cross bedding foresets. Eucalyptus trees and grasses cover the modern surface, and the uppermost 30 cm of the pit is dark clayey silty soil with abundant plant roots (Fig. 4). Throughout the section, plant roots are preserved as amorphous silica or magnesite casts (Fig. 4).

Bulbous cauliflower- or knuckled-finger-shaped magnesite nodules ranging from mm to 30 cm in diameter locally replace cross-bedded and laminated sediments but do not disturb adjacent sedimentary structures (Fig. 4). Trough cross-bed foresets with the most magnesite nodules also contain the highest abundances of authigenic clay. Incipient soft magnesite nodules contain abundant sand grains.

Micro-XRF maps reveal that some magnesite nodules exhibit concentric geochemical zoning (Fig. 5). Zonation can be either abrupt or gradational (Fig. 5). These nodules are milky white and span from hard and porcelaneous magnesites to softer, chalky varieties. Some magnesite nodules are white and pure in the center but become progressively contaminated with remnant sand or feldspar grains or authigenic halite and dolomite crystals towards the rim (Fig. 5). Iron and manganese oxides/hydroxides and cryptocrystalline silica may also encrust the exteriors of nodular magnesites and infiltrate along veins into the contaminated rims (e.g., Figs. 4f, and 5a and f).

4.2. *Major, minor and trace element chemistry*

4.2.1. *Serpentinites, weathered serpentinites, and magnesite veins at Gumigil*

Major, minor and trace element geochemistry for all samples and subsamples investigated in this study are presented in Table S1. At the Gumigil Mine, serpentinites become progressively more weathered from depth to the surface, where they become completely replaced by iron-silica (plus Cr-Al-Ti-Na) duricrusts (Figs. 2, 3 and 6). Serpentinite weathering is accompanied by a significant change in colour (iron oxidation) and increase in porosity (Figs. 2 and 3). MgO contents decrease progressively, until the Mg-depleted Fe-Si-Al-Ti-Cr-Na-rich duricrust is formed (Fig. 6a). In addition, Na contents increase with weathering intensity from the serpentinites to the ferricretes (Fig. 6b). Magnesite veins undergo Mg^{2+} loss, become progressively silicified, and are eventually completely replaced by supergene silica veins.

Chondrite-normalized REE spider diagrams for samples analyzed by total digestion show that Gumigil serpentinites are depleted respect to chondritic values of McDonough and Sun (1995) (Fig. 7). Co-existing magnesite veins analyzed by total digestion show even lower REE concentrations than the serpentinites, and magnesite-specific digestion show the lowest REE concentrations.

4.2.2. *Sand, magnesites, and Mn-oxides at Yaamba*

Pure Yaamba sediments devoid of carbonates were not analyzed, but sediments slightly cemented by magnesite (YP4–19-02, Table S1) document the arkosic composition of the sands (high Si, Al, K, and Na) (Table S1, Figs. 6 and 7).

Yaamba magnesites analyzed by both total and magnesite-specific

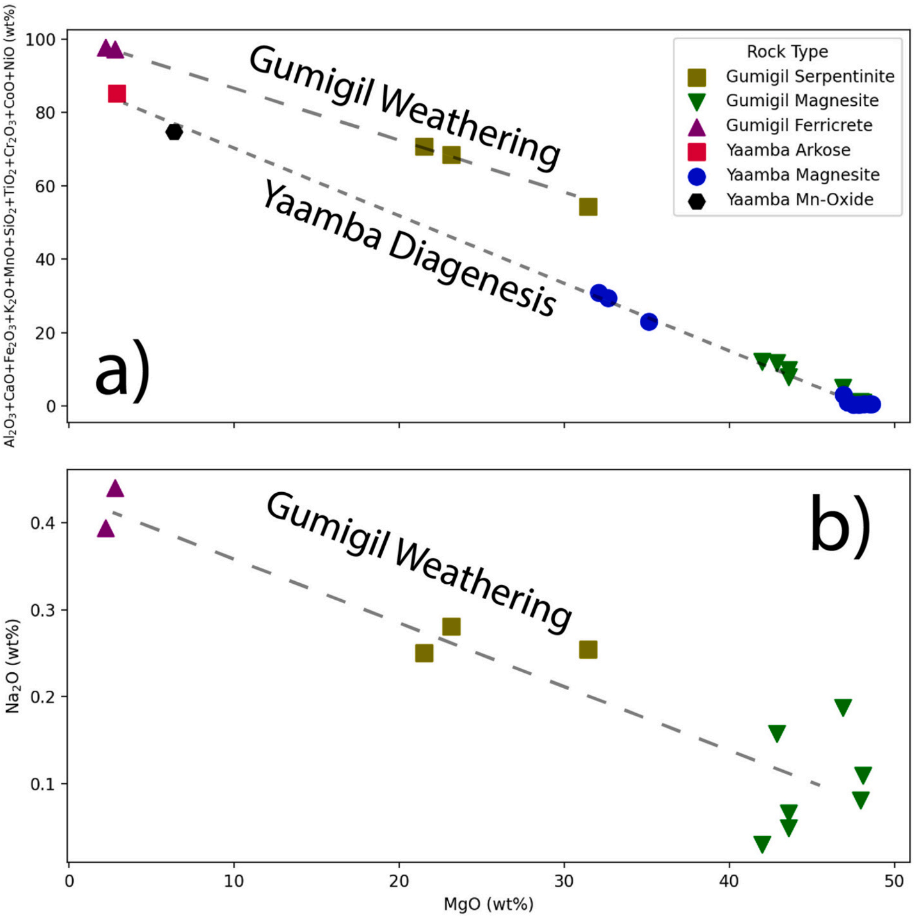

Fig. 6. Major and trace element chemical trends with shifts in MgO wt% during Gumigil Weathering (long-dashed line) and Yaamba Diagenesis (short-dashed line) from whole rock chemistry. Only data from Gumigil is shown in Panel B.

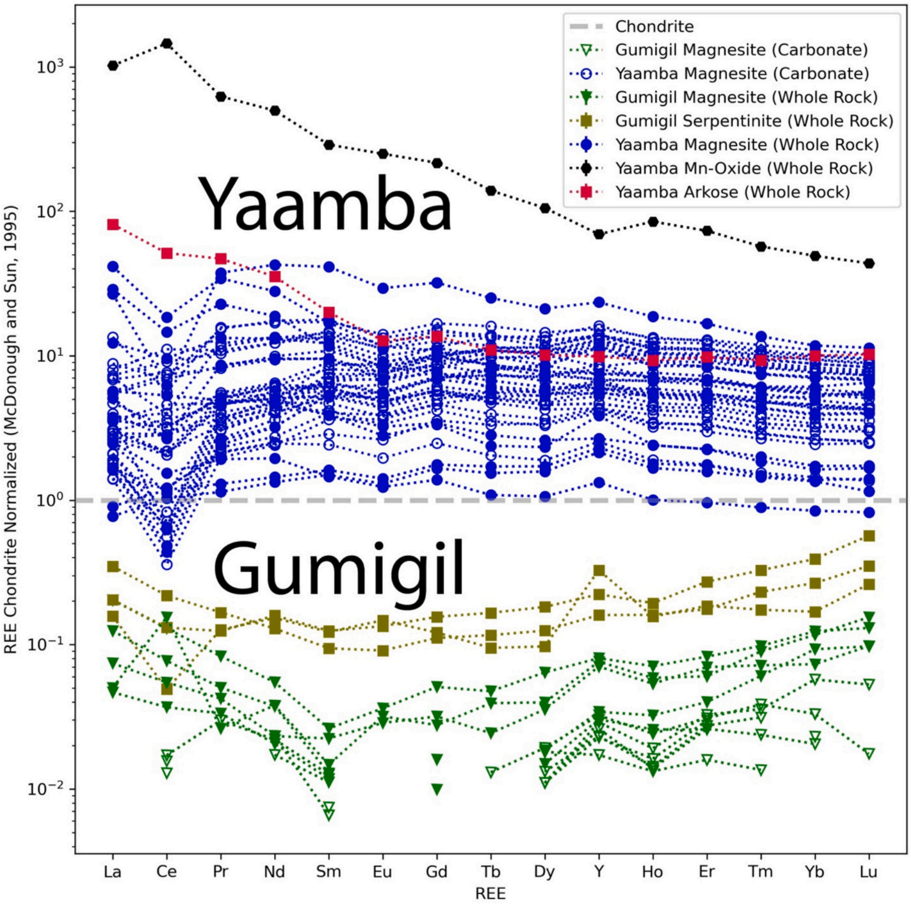

Fig. 7. Rare Earth element spider diagrams for samples from Gumigil and Yaamba. Whole rock analyses with serpentinite mixed with magnesite are labeled serpentinite for simplicity.

digestions show REE element enrichment with respect to chondritic values, except for the negative Ce-anomaly in many of the samples (Fig. 7). Importantly, magnesites from Yaamba have up to two-orders of magnitude higher REE contents than those from Gumigil, clearly distinguishing the two types of magnesites. Yaamba magnesites are depleted in LREE with respect to hosting sands, but most magnesites show HREE compositions similar to, or slightly depleted compared to the hosting sands (Fig. 7). Yaamba magnesites analyzed by the total digestion method show a broader dispersion in REE values than those analyzed by magnesite-specific digestions (Fig. 7). Most of the magnesite samples analyzed by either total or magnesite-specific digestion show pronounced negative Ce anomalies, but some samples show slightly positive anomalies. For comparison, Mn oxides in overlying soils show significant REE enrichment and a significant positive Ce anomaly when compared with the underlying carbonates and sediments (Fig. 7).

4.2.3. *Fractionation of Ce and Y*

As discussed above, chondrite normalized spider diagrams (Fig. 7) reveal that some samples have anomalous Ce and Y contents with respect to the general REE trend. To quantify these anomalies, we define Ce anomaly (Ce*) as

$$Ce^{*} = 2\left(\frac{Ce_N}{La_N + Pr_N}\right)$$

(Bau and Dulski, 1996) and Y anomaly (Y*) as

$$Y^{*} = \frac{Y_N}{Ho_N}$$

where the element with N subscript is the concentration of the REE or Y in the sample normalized to chondritic values reported by McDonough and Sun (1995). Values of Ce* and Y* greater or less than one indicate either enrichment (positive anomaly) or depletion (negative anomaly) of Ce or Y compared to the other REEs.

Two serpentinite samples from Gumigil have Y* and Ce* values close to one (Fig. 7; Table S1), but one sample (GUM 19–03) shows significant anomalies: $Y^* = 2.1$ and $Ce^* = 0.34$ (Fig. 7; Table S1). Magnesite veins from Gumigil all have positive Y* (Y* spans 1.04–1.88, Table S1). Ce* for magnesite veins analyzed by total digestion are close to one; Ce* could not be calculated for samples analyzed by magnesite-specific digestion because concentrations of La and Pr in the veins are below the limits of quantification.

The host arkosic sands at Yaamba do not display Ce or Y anomalies. The Yaamba magnesites have variable Ce*, which spans from slightly above one to sharply negative values (Ce* spans 0.16–1.17, Table S1). They also have variable Y*, which spans from slightly below one to positive values (Y* spans 0.92–1.6, Table S1). Importantly, Ce anomalies are positively correlated with Mn (Figs. 8 and 9). The correlation between Ce* with Mn among Yaamba magnesite samples is particularly noticeable in nodule samples where specific areas (cores and rims) were microsampled and analyzed by magnesite-specific digestions. Rims that have elevated Mn concentrations also have higher Ce* values and lower Y* values than the cores (Figs. 8 and 9). The Fe/Mn-oxides/hydroxides from Yaamba also show strongly positive Ce* and negative Y* values (Fig. 7, Table S1).

Among other REEs, Eu is redox sensitive under geological conditions, transitioning from Eu^{3+} to Eu^{2+} in reducing environments (Sverjensky, 1984). This does not tend to occur under near-surface conditions on Earth except for in extremely reducing conditions (log $fO_2 < -60$:

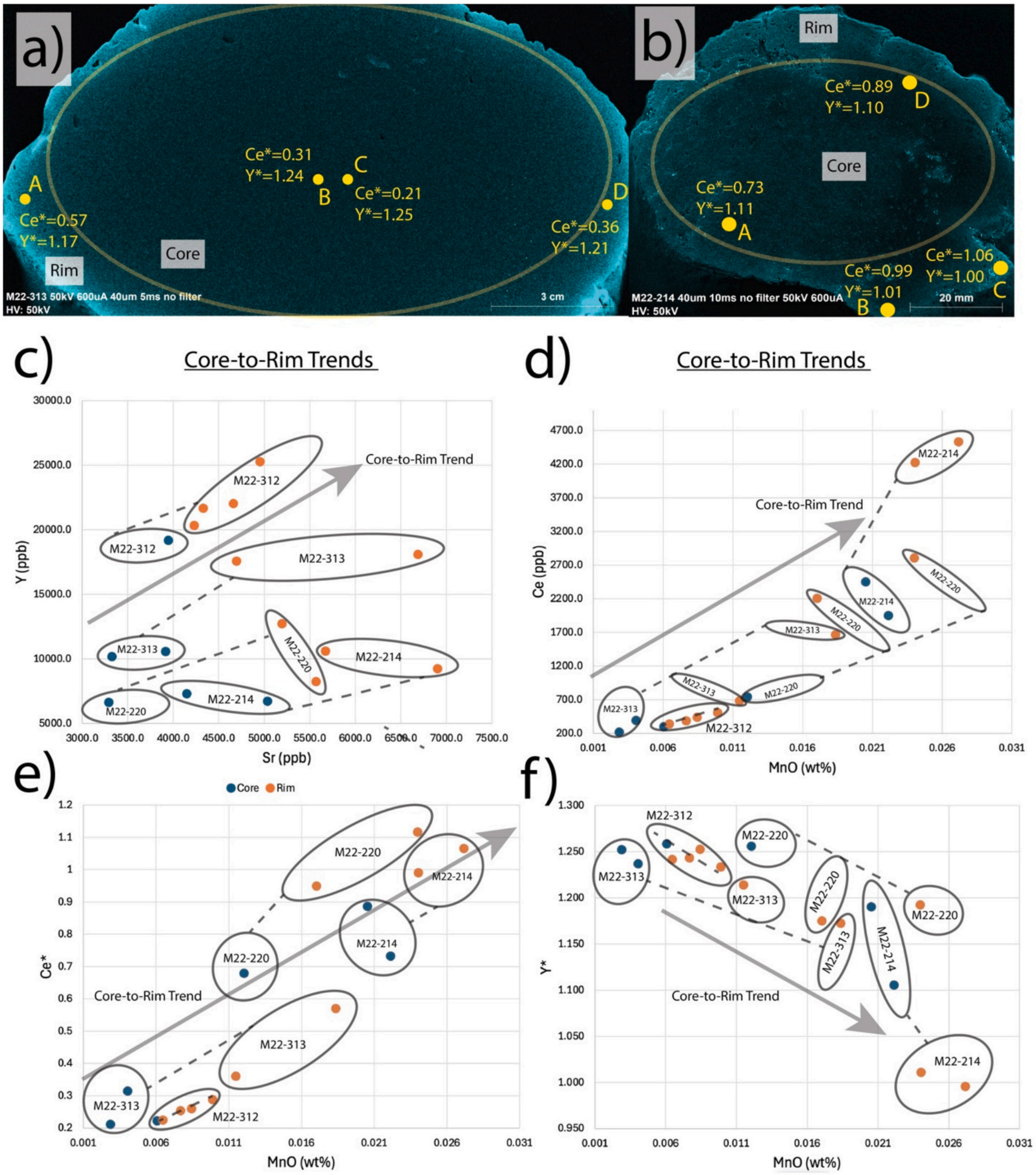

Fig. 8. Core-to-rim geochemical trends in four magnesite nodules from Yaamba (M22–214, M22–220, M22–312, and M22–313). Panels A and B show µXRF images of Mn zoning (bluer regions have to more Mn) in slabs cut from M22–313 and M22–214 respectively. Both Ce* and Y* are shown in regions where targeted carbonate-specific trace element analyses were conducted. Panels C—F are scatterplots showing geochemical relationships between the cores and rims of the zoned nodules. Grey arrows highlight the Core-to-Rim trends.

Sverjensky, 1984), and unlike Ce and Y, no significant deviations of Eu compared to other REEs are expressed by trace element data from Yaamba and Gumigil (Fig. 7).

5. Discussion

5.1. Formation and alteration of magnesite veins at Gumigil

To first order, magnesite veins at Gumigil share many geochemical features with the serpentine host rock. Serpentinite samples from Gumigil display low total REE concentrations and a slight MREE depletion (Fig. 7), similar to other Princhester Serpentinite bodies in the region (Bruce et al., 2000; Murray, 2007). These REE patterns are consistent with the signatures of depleted mantle-derived rocks elsewhere (e.g., Chen et al., 2019; Lian et al., 2017). The positive Y and negative Ce anomalies in one of the serpentinite samples (Fig. 7) most likely results from late-stage weathering effects, including staining and cementation by Fe/Mn-oxides/hydroxides which tend to preferentially incorporate oxidized cerium (Ce^{4+}) and reject Y relative to other REEs (Laveuf and Cornu, 2009; Thompson et al., 2013).

REE patterns in magnesite veins are even more depleted with respect to chondritic values than the host serpentinites, and they show a more pronounced MREE depletion and significantly positive Y anomalies (Fig. 7; Table S1). These REE patterns suggest that metamorphic magnesite veins formed by Mg^{2+} dissolution during reactive transformation of olivine, orthopyroxene, and clinopyroxene to serpentine, all of which are minerals present in the Gumigil profile. Relatively immobile REE (with respect to magnesium) remained in serpentine alteration products (e.g., Fe-Mn-oxdies/hydroxides), while coexisting vein magnesites became depleted in those elements. Interestingly, Y partitioned into the metamorphic or weathering solutions more than other REEs, enriching the magnesites at Gumigil (Fig. 7). More

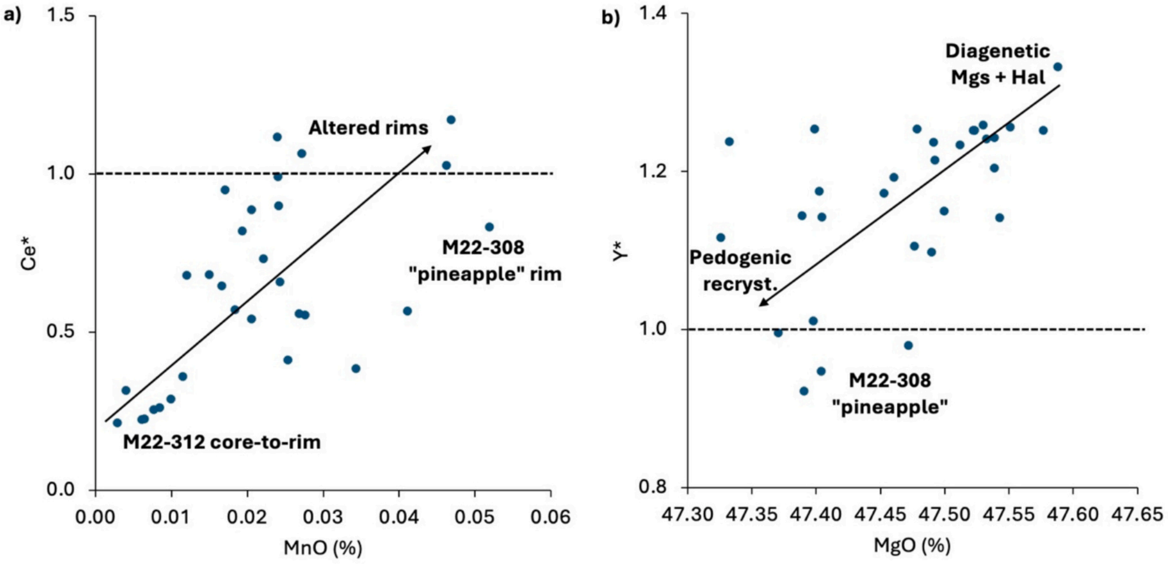

Fig. 9. REE fractionation of carbonate fraction in magnesite nodules at Yaamba mine. Panel a shows Cerium anomaly (Ce*) is negative in diagenetic magnesites, and values increase as magnesite rims recrystallize in the presence of reducing pedogenic fluids with mobile Mn and Ce. A pineapple-textured silicic rind on M22–308 shows more evidence of magnesite dissolution than recrystallization. Panel b shows Yttrium anomaly (Y*) is highest in diagenetic magnesite associated with halite, formed from evapotranspiration of groundwater, and diminishes with recrystallization in the presence of soil waters.

specifically, the positive Y* values of the magnesites may have resulted from mechanisms associated with supergene or surficial weathering processes associated with iron oxide formation (e.g., Thompson et al., 2013) or inheritance of positive Y* values from alkaline fluids during serpentinization (Kraemer et al., 2021). The fault-bound hierarchical vein networks of magnesite in the Gumigil serpentinites and their REE compositions (similar to Gumigil serpentinite: Fig. 7) indicate that veins formed by rock interaction with metasomatic fluids associated with serpentinization, rather than by supergene weathering (Iyer et al., 2008; Uno et al., 2022). This is a key distinction from other magnesite occurrences in serpentinites elsewhere in the New England Orogen, eastern Australia, which are interpreted to have formed in serpentinite saprolites (Oskierski et al., 2013a; Oskierski et al., 2013b; Oskierski et al., 2019) or as part of metamorphic aureoles associated with younger intrusions (Ashley and Brownlow, 1993). However, given that the positive Y* values are not ubiquitous among Gimigil serpentinites, it is more likely that they became expressed in magnesites and serpentinites from Gumigil as a result of supergene alteration.

5.2. Serpentinites as aqueous Mg^{2+} sources in groundwater: elemental losses and gains during weathering

The progressive enrichment in SiO_2 and Fe_2O_3 with simultaneous depletion in MgO in serpentinites (Fig. 6) is consistent with the expected lateritization trends documented in the region (Foster and Eggleton, 2002; Wilcock, 2000; Zeissink, 1969). In addition, Gumigil magnesites become progressively enriched in Si, Ni, and Na, while Mg^{2+} is lost to weathering solutions (Fig. 6) (Eggleton et al., 2011; Foster and Eggleton, 2002). This is noticeable on µXRF maps showing NaCl-rich (halite) rims on partially weathered and silicified magnesite veins (Fig. 3h). While Si enrichment results from local reactions, halite enrichment likely results from the introduction of marine-derived Na and Cl from atmospheric aerosols. The coexistence of halite and dolomite exclusively in weathered exteriors of metamorphic magnesite veins also suggests that Ca only becomes mobile and concentrated in solutions during the late stages of weathering, when most Mg^{2+} has already been leached from weathering-prone serpentine, olivines and orthopyroxenes, and relatively more weathering-resilient clinopyroxenes begin to dissolve in the saline and corrosive NaCl-rich weathering solutions. Calcium released from weathering clinopyroxenes migrates downward in the system, and it metasomatizes the outer walls of metamorphic magnesite veins, producing small amounts of supergene dolomite. Importantly, weathering trends document the massive export of aqueous Mg^{2+} from the serpentinite ridges into the surrounding plains (Foster and Eggleton, 2002).

5.3. The sinks: diagenetic and pedogenic reactions

While magnesites at Gumigil formed during serpentinization of ultramafic rocks at depth, magnesites at Yaamba formed from Mg^{2+}-rich groundwaters in the near-surface environment. REE patterns clearly distinguish metamorphic magnesites formed during serpentinization from the diagenetic magnesites replacing sediments in the basins (Fig. 7). In contrast with the metamorphic magnesites, diagenetic magnesites are slightly to significantly enriched in REEs with respect to chondritic values, show slight LREE and HREE depletion relative to MREE, and mostly display pronounced negative Ce anomalies (Figs. 7 and 9; Table S1). These results are explained by a model in which magnesium leached during weathering of serpentinites migrated in groundwater into the surrounding low-lying sedimentary deposits, ascended towards the surface in the capillary zone atop an unconfined aquifer, reacted and dissolved unconsolidated sediments, and replaced these sediments with diagenetic magnesites. Diagenetic magnesites acquired trace element signatures inherited from the sediments dissolved to make space for the newly formed carbonates (Fig. 7).

The sediments from Yaamba have far higher REE and Y concentrations than the serpentinites and are LREE enriched compared to a flat chondrite normalized REE pattern (Fig. 7). This is consistent with sedimentary and differentiated crustal rocks (e.g., Jiang et al., 2019; Pourmand et al., 2012; Shkol'nik et al., 2011; Yusheng et al., 2006). Congruent dissolution of detrital silicates, as is the case for magnesites replacing arkoses at Yaamba, increases the dissolved REE contents of local groundwaters. The MREE/HREE ratios (e.g., Dy/Lu) of Yaamba magnesites span to encompass the values of the host sediments or are very close (e.g., Dy/Yb), suggesting that the sediments are the primary source of the REEs in the magnesites.

However, most diagenetic magnesites have lower REE concentrations than the sediments that they replace (Fig. 7). This important relationship illustrates that the groundwaters responsible for magnesite precipitation and sediment dissolution export REEs upwards towards the surficial, dark, clay-rich vertisol soils at the top of the profile. The strong negative Ce anomaly in many magnesite samples thus reflects preferential retention of Ce in Fe/Mn-oxides/hydroxides soil horizons compared to other REEs. The ascending groundwaters were likely reducing, circumneutral, and silica-poor fluids that could transport trivalent Ce. The strongly REE-enriched manganese pisoids in this uppermost horizon illustrates how upwardly-mobile Ce, REEs and redox-sensitive elements accumulated in uppermost soils with Mn- and Fe-oxides (Laveuf et al., 2012; Laveuf and Cornu, 2009; Pédrot et al., 2015; Ratié et al., 2023). Cyclic fluid flow from the lower to upper horizons and back during the initial stages of magnesite formation coupled with the oxidative scavenging of Ce^{4+} in the upper horizons by Fe/Mn-oxides/hydroxides compared to other REEs resulted in the low Ce* values in the cores of zoned magnesites and high Ce* in the manganese pisoids.

In addition, the LREE/HREE (e.g., Nd/Yb) ratios of the magnesites at Yaamba are lower than those of the host sediments (Table S1), which indicates that LREE fractionation occurs during dissolution of the arkosic sands or during magnesite precipitation. Lattice-driven preferential rejection of LREEs may influence the REE signatures of the magnesites (Fernandez-Nieto et al., 2003; Kilias et al., 2006; Lugli et al., 2000). This is a key distinction between groundwater-formed diagenetic magnesites and other terrestrial diagenetic carbonates: magnesite preferentially rejects LREEs compared to dolomite and calcite due to the smaller ionic radius of octahedral Mg^{2+} compared to Ca^{2+} in carbonates (Fernandez-Nieto et al., 2003; Kilias et al., 2006; Lugli et al., 2000). The LREE dissolved from the corroding sands appear to remain in the ascending solutions and eventually coprecipitate with the Fe/Mn-oxides/hydroxides at the bottom of overlying soil layers.

As the authigenic soil horizon developed atop the sands coincident with their replacement by magnesite, infiltrating soil fluids began to interact with groundwaters at the top of the capillary zone. Carbonic or organic acids produced by vegetation dissolved the redox-sensitive elements enriched in the Mn and Fe-oxides. The descending soil solutions reacted with the previously formed magnesite nodules. Redox-sensitive elements from the dissolved oxides became incorporated into pedogenic alteration rims of the magnesite nodules, which accordingly exhibit elevated Ce* (sometimes $Ce^* > 1$) and Mn concentrations and low Y* compared to the diagenetic cores (Fig. 8). Trends in Ce*, Y* and Mn concentrations in the oxides, magnesites, and host sediments collectively indicate their values in the zoned Yaamba nodules are governed by the simultaneous precipitation of magnesite under reducing conditions at depth and Mn-Fe-oxides under oxidizing conditions near the water table. Coupling between magnesite and Mn-Fe-oxide precipitation is necessary to produce the Ce*, Y*, and Mn trends observed in the magnesite nodules at depth and the Mn—Fe oxides in soil horizons.

5.4. *Cryptocrystalline magnesites as tracers of late-stage retrograde reactions*

The likely corrosive nature of the strongly alkaline fluids ($pH \geq 8.5$: Barakat et al., 2022; Brookins, 1988) that carry excess Mg^{2+} in solution, either under metamorphic or supergene conditions, results in the formation of pure $MgCO_3$ devoid of other phases (e.g., silicates, phosphates, detrital oxides). Contrary to other diagenetic or supergene phases such as gypsum or calcite, that often form large crystals, magnesite in low-grade metamorphic rocks or sedimentary environments is invariably cryptocrystalline, homogeneous, and pure, but rich in nanoscale porosity. The porous, cryptocrystalline, and mineralogically pure magnesite veins and nodules, combined with the chemical reactivity of carbonates renders these samples as sensitive reaction vessels that record compositions that reflect the trace element characteristics of solutions that migrate through a magnesite-bearing system after mineral precipitation. In our study, both metamorphic and diagenetic magnesites undergo notable late-stage alteration by descending weathering solution, which are evident from the pedogenic alteration rims on magnesite veins and nodules documented by X-ray fluorescence maps (Fig. 5). Some of the rims become enriched in NaCl (halite) and Ca-rich supergene magnesite. Negative Ce anomalies and positive Y anomalies in magnesites, which indicated formation in reducing fluids that interacted with oxic horizons, become progressively less pronounced in rims than in the pure magnesite cores. Ce anomalies eventually become slightly positive, consistent with the re-introduction of Ce, together with aqueous Mn and Fe, by descending soil solutions (Fig. 8). Lattice bound Mn in the zoned magnesite nodules increase from core to rim (Fig. 8). As pedogenic solutions infiltrated into the outer walls of porous cryptocrystalline magnesite veins or nodules, the solutions reacted with and partially dissolved the diagenetic magnesite and became alkaline, driving the generation of recrystallized magnesite now rich in Mn and Ce (Fig. 10).

5.5. *Relevance to Mars exploration*

The ultramafic highlands and the low-lying fluvial basins of the Marlborough terrain in Queensland, Australia, are lithologically and topographically analogous to Jezero crater, Mars. Trace element and isotopic signatures in chemically distinct carbonate zones in terrestrial and Martian Mg-carbonates (Eiler et al., 2002; Oskierski et al., 2013b) could record thermal histories, redox conditions, age, fluid source and more.

Mg-carbonates exposed in aqueously altered igneous rocks on the Martian surface, such as those detected and sampled by Perseverance during the Mars 2020 mission (Clavé et al., 2023; Farley et al., 2022; Scheller et al., 2022), may host information on the composition and possible temperatures of the aqueous reactions that produced the carbonates. If carbonates were produced by metamorphic reactions within the host ultramafic rocks, they will have compositions and REE patterns reflecting those of the hosting ultramafic units, similarly to Gumigil. If Jezero crater Mg-carbonates were produced from near-surface aqueous alteration (Stack et al., 2024), they should record Martian redox environmental conditions at the time of carbonate precipitation.

For Martian meteorite ALH84001, both 1) thermal histories constraining two stages of carbonate formation (~190 °C for concretion cores and ~ 20 °C for magnesite rims: from Sr/Ca ratios and $\delta^{18}O$) and 2) geochronological constraints on carbonate precipitation (4.04 ± 0.10 Gya from a Pb—Pb isochron and 3.90 ± 0.04 Gya from a Rb—Sr isochrons) have been placed (Borg et al., 1999; Eiler et al., 2002). While concentrations of Y, La, Ce and Nd in ALH84001 carbonates determined by secondary ionization mass spectrometry indicate that carbonate cores tend to have lower Ce concentrations relative to other measured REEs compared to the rims (similar to the cores and rims of the Yaamba magnesite nodules: see Fig. 8), analytical uncertainties were not well constrained and no data is presented for the coexisting iron oxides, complicating the interpretability of the data (Eiler et al., 2002).

REE concentrations in the ALH84001 carbonates are about one to two orders of magnitude higher than those of magnesite samples from Gumigil (Eiler et al., 2002). If Martian carbonates in samples retrieved by *Perseverance* are compositionally similar to those of ALH84001, low abundances should not be problematic. Trace element contents of these magnesites could place constraints on the redox potential of the ancient Martian atmosphere billions of years ago. As is the case with differentiated and ultramafic rock units on Earth, variability in Martian source rock must be considered (Deschamps et al., 2013; McLennan, 2001; Norman, 1999).

If these carbonates formed early in the history of aqueous alteration of the ultramafic igneous rocks at the Martian surface and have remained on the Martian surface since their formation, they may also record post precipitation aqueous events, similarly to that observed at both Gumigil and Yaamba. For example, the precipitation of atmospherically produced perchlorates (Catling et al., 2010) or dust-derived sulfur species and their subsequent remobilization by transient water

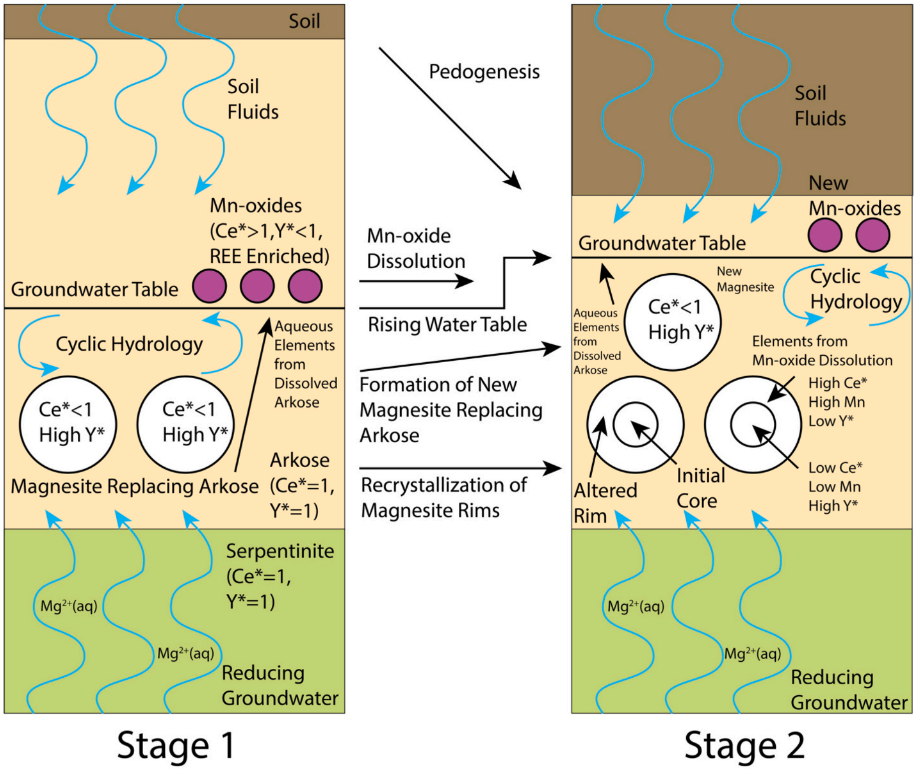

Fig. 10. A two-stage formation process highlighting events associated with prograde magnesite formation (diagenesis) and retrograde alteration rims (recrystallization) at Yaamba. Interactions associated with the formation, alteration and dissolution of magnesites (white), serpentinites (green), Mn-oxides (purple), soil (brown) and arkose (tan), coupled with the aqueous mobility of dissolved ions through pore fluids (blue) lead to the geochemical signatures preserved in the samples from Yaamba. The Ce* and Y* of the Arkose and serpentinite are shown as equal to one for simplicity (less fractionated relative to chondrite) as the Y and Ce fractionation compared to other REEs is less extreme in these samples compared to the magnesites and Mn-oxides (Fig. 7). (For interpretation of the references to colour in this figure legend, the reader is referred to the web version of this article.)

cycling would have produced reaction rims on Martian magnesites similar to those produced by late-stage weathering rims at both Gumigil and Yaamba. Thus, a 10-cm long drill core of a Jezero crater ultramafic sample that contains carbonates from the surface down may represent a reaction vessel that records aqueous conditions at the time of carbonate precipitation at the bottom, and the compositions of superimposed aqueous solutions that may have altered the original carbonates at the near-surface drill-core top. Following the Mars Sample Return mission, detailed downhole trace element mapping and analyses of Martian magnesites and co-precipitated phases could shed light on water-rock interactions and shifts in redox conditions that took place on the Martian surface throughout the entire history of exposure of the igneous rocks currently blanketing Jezero crater.

6. Conclusion

The Gumigil and Yaamba mines in Queensland, Australia, represent sources and sinks for Mg^{2+} ions, respectively. Magnesium sources at Gumigil are serpentinities and metamorphically produced magnesite veins. While field observations indicate that magnesites at Gumigil were produced at depth under high fluid pressures associated with serpentinization, lateritic weathering processes have influenced the trace element geochemistry of visibly pristine magnesite samples. The trace element geochemistry of magnesites at Gumigil are compatible with a metamorphic origin with late-stage alteration by weathering. In particular, REE geochemistry suggest the formation of magnesite veins in equilibrium with serpentinites and strongly depleted with respect to chondritic REE patterns of McDonough and Sun (1995). Aqueous Mg^{2+} exported from weathering of serpentinites and magnesite veins at Gumigil and from other serpentinite ridges was introduced into fluvial sedimentary basins hosting arkosic sediments sourced from nearby granitic and metamorphic rocks. As Mg^{2+}-bearing groundwaters approached the main river draining the region (the Fitzroy River), the hydraulic head created by differences in elevation between the serpentinite ridges and fluvial plains drove the solutions nearer to the surface. As Mg^{2+}-bearing groundwaters ascended and evaporated, the fluids became alkaline, resulting in congruent dissolution of detrital quartz and feldspars and subsequent precipitation of overlying metal oxides and authigenic clays in vertisol soils. In the process, sediments were diagenetically replaced by magnesite, producing magnesite cements, concretions, nodules, and pinnacles, and authigenic Mg^{2+}-bearing clays (all magnesium sinks at Yaamba). Trace element geochemistry reveals a strong influence of dissolving crustal rocks; in particular, chondrite-enriched REE enrichment with respect to chondritic values of McDonough and Sun (1995) confirm a dominant crustal component contribution to the authigenic magnesites at Yaamba. Magnesite initially forms diagenetically by ascending reduced solutions that export REEs to upper horizons. In the upper horizons, Fe/Mn-oxides/hydroxides preferentially retained oxidized Ce compared to other REEs, which remained in solution as trivalent cations that interacted with the primary carbonates via cyclic fluid flow between the lower reduced horizons and the upper oxidized horizons. Later in the system's history, descending soil solutions reintroduce Ce, Mn, and Fe, forming rims with elevated Ce anomalies on the outer walls of magnesite nodules. The mechanisms of formation and trace element geochemistry of Gumigil and Yaamba magnesites provide a useful analog for the formation of Mg-carbonates at Jezero crater, Mars.

CRediT authorship contribution statement

Carl Swindle: Writing – review & editing, Writing – original draft, Visualization, Validation, Methodology, Investigation, Funding acquisition, Formal analysis, Data curation, Conceptualization. **Paulo Vasconcelos:** Writing – review & editing, Writing – original draft, Visualization, Validation, Supervision, Resources, Project administration, Methodology, Investigation, Funding acquisition, Formal analysis, Data curation, Conceptualization. **Zoe Dimarco:** Writing – review & editing, Writing – original draft, Visualization, Validation, Methodology, Investigation, Formal analysis, Data curation, Conceptualization. **Nathan Dalleska:** Writing – review & editing, Writing – original draft, Visualization, Validation, Supervision, Software, Resources, Methodology, Investigation, Formal analysis, Data curation. **Ai Nguyen:** Writing – review & editing, Writing – original draft, Validation, Resources, Methodology, Investigation, Formal analysis, Data curation. **Emily Cardarelli:** Writing – review & editing, Writing – original draft, Investigation. **Surjyendu Bhattacharjee:** Writing – review & editing, Writing – original draft, Investigation. **Kenneth Farley:** Writing – review & editing, Writing – original draft, Visualization, Supervision, Project administration, Methodology, Investigation, Funding acquisition, Conceptualization. **Theodore Present:** Writing – review & editing, Writing – original draft, Visualization, Validation, Supervision, Project administration, Methodology, Investigation, Formal analysis, Data curation, Conceptualization.

Declaration of competing interest

The authors declare the following financial interests/personal relationships which may be considered as potential competing interests:

Carl Swindle reports financial support was provided by National Science Foundation. Kenneth A. Farley reports financial support was provided by Simons Foundation. If there are other authors, they declare that they have no known competing financial interests or personal relationships that could have appeared to influence the work reported in this paper.

Acknowledgements

We thank QMag Pty. Limited and the Gumigil Chrysoprase Mine for sampling access. Peter Martin, Eva Scheller, Kenneth Williford, Kelsey Moore, and Eryn Eitel assisted sample collection in the field. This project benefited from the use of instrumentation made available by the Resnick Sustainability Institute's Water and Environment Lab at the California Institute of Technology, the Environmental Geochemistry Laboratory at the University of Queensland, the Centre for Microscopy and Microanalysis at the University of Queensland, and the Caltech Division of Geological and Planetary Science. This project was supported by Simons Foundation Project Award [668346] and the National Science Foundation Graduate Research Fellowship Grant [DGE-1745301] to Carl Swindle.

Appendix A. Supplementary data

Supplementary data to this article can be found online at https://doi.org/10.1016/j.chemgeo.2025.123068.

Data availability

Data is available in the manuscript and supplementary table.

References

Abrams, M., Yamaguchi, Y., Crippen, R., 2022. Aster global DEM (GDEM) version 3. Int. Arch. Photogramm. Remote. Sens. Spat. Inf. Sci. 593–598. https://doi.org/10.5194/isprs-archives-XLIII-B4-2022-593-2022. XLIII-B4-2022.

Alonso-Zarza, A.M., Wright, V.P., 2010a. Chapter 2 Palustrine carbonates. In: Developments in Sedimentology, vol. 61. Elsevier, pp. 103–131. https://doi.org/10.1016/S0070-4571(09)06102-0.

Alonso-Zarza, A.M., Wright, V.P., 2010b. Chapter 5 Calcretes. In: Developments in Sedimentology, vol. 61. Elsevier, pp. 225–267. https://doi.org/10.1016/S0070-4571(09)06105-6.

Ashley, P., Brownlow, J., 1993. Silica-carbonate alteration zones in the Great Serpentinite Belt, southern New England Orogen: their nature and significance. New England Orogen, Eastern Australia. In: Flood, P.G., Aitchison, J.C. (Eds.), Papers Presented at a Conference, Armidale, NSW, 2-4 February, 1993. University of New England. Department of Geology and Geophysics, Armidale, NSW. https://doi.org/10.3316/aesis.199409966.

Barakat, Y., Cui, Y.-J., Mokni, N., Delage, P., Bernier, F., 2022. Effects of pH and exposure time to alkaline solutions on the mineralogy of the Opalinus Clay from the lower sandy facies of Mont Terri site. Eng. Geol. 306, 106766. https://doi.org/10.1016/j.enggeo.2022.106766.

Bau, M., Dulski, P., 1996. Anthropogenic origin of positive gadolinium anomalies in river waters. Earth Planet. Sci. Lett. 143 (1–4), 245–255. https://doi.org/10.1016/0012-821X(96)00127-6.

Borg, L.E., Connelly, J.N., Nyquist, L.E., Shih, C.-Y., Wiesmann, H., Reese, Y., 1999. The age of the carbonates in Martian meteorite ALH84001. Science 286 (5437), 90–94. https://doi.org/10.1126/science.286.5437.90.

Brookins, D.G., 1988. Eh-pH Diagrams for Geochemistry. Springer Berlin Heidelberg. https://doi.org/10.1007/978-3-642-73093-1.

Bruce, M.C., Niu, Y., Harbort, T.A., Holcombe, R.J., 2000. Petrological, geochemical and geochronological evidence for a Neoproterozoic Ocean basin recorded in the Marlborough terrane of the northern New England Fold Belt. Aust. J. Earth Sci. 47 (6), 1053–1064. https://doi.org/10.1046/j.1440-0952.2000.00833.x.

Cao, C., Liu, X.-M., Bataille, C.P., Liu, C., 2020. What do Ce anomalies in marine carbonates really mean? A perspective from leaching experiments. Chem. Geol. 532, 119413. https://doi.org/10.1016/j.chemgeo.2019.119413.

Caravaca, G., Dromart, G., Mangold, N., Gupta, S., Kah, L.C., Tate, C., Williams, R.M.E., Le Mouélic, S., Gasnault, O., Bell, J., Beyssac, O., Nuñez, J.I., Randazzo, N., Rice, J., Crumpler, L.S., Williams, A., Russel, P., Stack, K.M., Farley, K.A., Wiens, R.C., 2024. Depositional facies and sequence stratigraphy of Kodiak Butte, Western Delta of Jezero Crater, Mars. J. Geophys. Res. Planets 129 (4), e2023JE008205. https://doi.org/10.1029/2023JE008205.

Catling, D.C., Claire, M.W., Zahnle, K.J., Quinn, R.C., Clark, B.C., Hecht, M.H., Kounaves, S., 2010. Atmospheric origins of perchlorate on Mars and in the Atacama. J. Geophys. Res. Planets 115 (E1), 2009JE003425. https://doi.org/10.1029/2009JE003425.

Chen, L., Tang, L., Li, X., Dong, Y., Yu, X., Ding, W., 2019. Geochemistry of peridotites from the Yap Trench, Western Pacific: implications for subduction zone mantle evolution. Int. Geol. Rev. 61 (9), 1037–1051. https://doi.org/10.1080/00206814.2018.1484305.

Clavé, E., Benzerara, K., Meslin, P.-Y., Forni, O., Royer, C., Mandon, L., Beck, P., Quantin-Nataf, C., Beyssac, O., Cousin, A., Bousquet, B., Wiens, R.C., Maurice, S., Dehouck, E., Schröder, S., Gasnault, O., Mangold, N., Dromart, G., Bosak, T., the SuperCam team, 2023. Carbonate detection with SuperCam in igneous rocks on the floor of Jezero Crater, Mars. J. Geophys. Res. Planets 128 (6), e2022JE007463. https://doi.org/10.1029/2022JE007463.

Croke, J., Jansen, J.D., Amos, K., Pietsch, T.J., 2011. A 100 ka record of fluvial activity in the Fitzroy River Basin, tropical northeastern Australia. Quat. Sci. Rev. 30 (13–14), 1681–1695. https://doi.org/10.1016/j.quascirev.2011.03.012.

De Deckker, P., 2019. Groundwater interactions control dolomite and magnesite precipitation in saline playas in the Western District Volcanic Plains of Victoria, Australia. Sediment. Geol. 380, 105–126. https://doi.org/10.1016/j.sedgeo.2018.11.010.

Deschamps, F., Godard, M., Guillot, S., Hattori, K., 2013. Geochemistry of subduction zone serpentinites: a review. Lithos 178, 96–127. https://doi.org/10.1016/j.lithos.2013.05.019.

Eggleton, R.A., Fitz Gerald, J., Foster, L., 2011. Chrysoprase from Gumigil, Queensland. Aust. J. Earth Sci. 58 (7), 767–776. https://doi.org/10.1080/08120099.2011.594091.

Eiler, J.M., Valley, J.W., Graham, C.M., Fournelle, J., 2002. Two populations of carbonate in ALH84001: geochemical evidence for discrimination and genesis. Geochim. Cosmochim. Acta 66 (7), 1285–1303. https://doi.org/10.1016/S0016-7037(01)00847-X.

Elderfield, H., Greaves, M., Barker, S., Hall, I.R., Tripati, A., Ferretti, P., Crowhurst, S., Booth, L., Daunt, C., 2010. A record of bottom water temperature and seawater δ18O for the Southern Ocean over the past 440kyr based on Mg/Ca of benthic foraminiferal Uvigerina spp. Quat. Sci. Rev. 29 (1–2), 160–169. https://doi.org/10.1016/j.quascirev.2009.07.013.

Farley, K.A., Stack, K.M., Shuster, D.L., Horgan, B.H.N., Hurowitz, J.A., Tarnas, J.D., Simon, J.I., Sun, V.Z., Scheller, E.L., Moore, K.R., McLennan, S.M., Vasconcelos, P. M., Wiens, R.C., Treiman, A.H., Mayhew, L.E., Beyssac, O., Kizovski, T.V., Tosca, N. J., Williford, K.H., Zorzano, M.-P., 2022. Aqueously altered igneous rocks sampled on the floor of Jezero crater, Mars. Science 377 (6614), eabo2196. https://doi.org/10.1126/science.abo2196.

Fernandez-Nieto, C., Torres-Ruiz, J., Subias Perez, I., Fanlo Gonzalez, I., Gonzalez Lopez, J.M., 2003. Genesis of Mg-Fe carbonates from the Sierra Menera magnesite-siderite deposits, Northeast Spain: evidence from fluid inclusions, trace elements, rare Earth elements, and stable isotope data. Econ. Geol. 98 (7), 1413–1426. https://doi.org/10.2113/gsecongeo.98.7.1413.

Foster, L., Eggleton, R., 2002. The Marlborough nickel laterite deposits. In: Regolith and Landscapes in Eastern Australia, pp. 33–36.

Gahlan, H.A., Azer, M.K., Asimow, P.D., Mubarak, H.S., Al-Kahtany, K.M., 2020. Petrological characteristics of the Neoproterozoic Ess ophiolite mantle section, Arabian Shield, Saudi Arabia: a mineral chemistry perspective. Int. J. Earth Sci. 109 (1), 239–251. https://doi.org/10.1007/s00531-019-01799-3.

Giampouras, M., Garrido, C.J., Zwicker, J., Vadillo, I., Smrzka, D., Bach, W., Peckmann, J., Jiménez, P., Benavente, J., García-Ruiz, J.M., 2019. Geochemistry and mineralogy of serpentinization-driven hyperalkaline springs in the Ronda peridotites. Lithos 350–351, 105215. https://doi.org/10.1016/j.lithos.2019.105215.

Giampouras, M., Garrido, C.J., Bach, W., Los, C., Fussmann, D., Monien, P., García-Ruiz, J.M., 2020. On the controls of mineral assemblages and textures in alkaline springs, Samail Ophiolite, Oman. Chem. Geol. 533, 119435. https://doi.org/10.1016/j.chemgeo.2019.119435.

Halevy, I., Fischer, W.W., Eiler, J.M., 2011. Carbonates in the Martian meteorite Allan Hills 84001 formed at 18 ± 4 °C in a near-surface aqueous environment. Proc. Natl. Acad. Sci. 108 (41), 16895–16899. https://doi.org/10.1073/pnas.1109444108.

Iyer, K., Jamtveit, B., Mathiesen, J., Malthesorenssen, A., Feder, J., 2008. Reaction-assisted hierarchical fracturing during serpentinization. Earth Planet. Sci. Lett. 267 (3–4), 503–516. https://doi.org/10.1016/j.epsl.2007.11.060.

Jessop, K., Daczko, N.R., Piazolo, S., 2019. Tectonic cycles of the New England Orogen, eastern Australia: a review. Aust. J. Earth Sci. 66 (4), 459–496. https://doi.org/10.1080/08120099.2018.1548378.

Jiang, Z., Sun, Z., Liu, Z., Cao, H., Geng, W., Xu, H., Wang, L., Wang, L., 2019. Rare-earth element geochemistry reveals the provenance of sediments on the southwestern margin of the challenger deep. J. Oceanol. Limnol. 37 (3), 998–1009. https://doi.org/10.1007/s00343-019-8046-8.

Kaya, M., Yildirim, B.A., Kumral, M., Sasmaz, A., 2023. Trace and rare Earth element (REE) geochemistry of recently formed stromatolites at Lake Salda, SW Turkey. Water 15 (4), 733. https://doi.org/10.3390/w15040733.

Kelemen, P.B., Matter, J., 2008. In situ carbonation of peridotite for CO_2 storage. Proc. Natl. Acad. Sci. 105 (45), 17295–17300. https://doi.org/10.1073/pnas.0805794105.

Kilias, S.P., Pozo, M., Bustillo, M., Stamatakis, M.G., Calvo, J.P., 2006. Origin of the Rubian carbonate-hosted magnesite deposit, Galicia, NW Spain: mineralogical, REE, fluid inclusion and isotope evidence. Mineral. Deposita 41 (7), 713–733. https://doi.org/10.1007/s00126-006-0075-5.

Kraemer, D., Frei, R., Ernst, D.M., Bau, M., Melchiorre, E., 2021. Serpentinization in the Archean and early Phanerozoic – insights from chromium isotope and REY systematics of the Mg Cr hydroxycarbonate stichtite and associated host serpentinites. Chem. Geol. 565, 120055. https://doi.org/10.1016/j.chemgeo.2020.120055.

Lachniet, M.S., 2009. Climatic and environmental controls on speleothem oxygen-isotope values. Quat. Sci. Rev. 28 (5–6), 412–432. https://doi.org/10.1016/j.quascirev.2008.10.021.

Laveuf, C., Cornu, S., 2009. A review on the potentiality of rare Earth elements to trace pedogenetic processes. Geoderma 154 (1–2), 1–12. https://doi.org/10.1016/j.geoderma.2009.10.002.

Laveuf, C., Cornu, S., Guilherme, L.R.G., Guerin, A., Juillot, F., 2012. The impact of redox conditions on the rare earth element signature of redoximorphic features in a soil sequence developed from limestone. Geoderma 170, 25–38. https://doi.org/10.1016/j.geoderma.2011.10.014.

Lian, D., Yang, J., Liu, F., Wu, W., Zhang, L., Zhao, H., Huang, J., 2017. Geochemistry and tectonic significance of the Gongzhu peridotites in the northern branch of the western Yarlung Zangbo ophiolitic belt, western Tibet. Mineral. Petrol. 111 (5), 729–746. https://doi.org/10.1007/s00710-017-0491-5.

Liu, Y., Tice, M.M., Schmidt, M.E., Treiman, A.H., Kizovski, T.V., Hurowitz, J.A., Allwood, A.C., Henneke, J., Pedersen, D.A.K., VanBommel, S.J., Jones, M.W.M., Knight, A.L., Orenstein, B.J., Clark, B.C., Elam, W.T., Heirwegh, C.M., Barber, T., Beegle, L.W., Benzerara, K., Zorzano, M.-P., 2022. An olivine cumulate outcrop on the floor of Jezero crater. Mar. Sci. 377 (6614), 1513–1519. https://doi.org/10.1126/science.abo2756.

Lugli, S., Torres-Ruiz, J., Garuti, G., Olmedo, F., 2000. Petrography and geochemistry of the Eugui magnesite deposit(Western Pyrenees, Spain): evidence for the development of a peculiar zebra banding by dolomite replacement. Econ. Geol. 95 (8), 1775–1791. https://doi.org/10.2113/gsecongeo.95.8.1775.

Matheson, S.G., 1988. Oil shale resources and exploration in Queensland, 1986–1987. Fuel 67 (10), 1398–1400. https://doi.org/10.1016/0016-2361(88)90129-9.

McDonough, W.F., Sun, S.-S., 1995. The composition of the Earth. Chem. Geol. 120 (3–4), 223–253. https://doi.org/10.1016/0009-2541(94)00140-4.

McLennan, S.M., 2001. Relationships between the trace element composition of sedimentary rocks and upper continental crust. Geochem. Geophys. Geosyst. 2 (4), 2000GC000109. https://doi.org/10.1029/2000GC000109.

Mervine, E.M., Humphris, S.E., Sims, K.W.W., Kelemen, P.B., Jenkins, W.J., 2014. Carbonation rates of peridotite in the Samail Ophiolite, Sultanate of Oman, constrained through 14C dating and stable isotopes. Geochim. Cosmochim. Acta 126, 371–397. https://doi.org/10.1016/j.gca.2013.11.007.

Milburn, D., Wilcock, S., 1994. The Kunwarara magnesite deposit, Central Queensland. In: Field Conference '94 Capricorn Region: Geological Society of Australia, pp. 99–107.

Milburn, D., Wilcock, S., 1998. Kunwarara magnesite depsoit. In: Geology of Australian and Papua New Guinean Mineral Deposits, pp. 815–818.

Murray, C.G., 2007. Devonian supra-subduction zone setting for the Princhester and Northumberland Serpentinites: implications for the tectonic evolution of the northern New England Orogen. Aust. J. Earth Sci. 54 (7), 899–925. https://doi.org/10.1080/08120090701392747.

Murray, C.G., Barker, R.M., Blake, P.R., Burrows, P.E., Crouch, S.B.S., Fordham, B.G., Hayward, M.A., Livingstone, M.D., Morwood, D.A., Parfrey, S.M., Robertson, A.D.C., Simpson, G.A., 1997. The Yarrol project—increasing the prospectivity of the New England Orogen in the Rockhampton-Monto Region, central coastal Queensland. In: Proceedings of the Queensland Development 1997 Conference. Queensland Department of Mines and Energy, Brisbane, pp. 39–56.

Norman, M.D., 1999. The composition and thickness of the crust of Mars estimated from rare earth elements and neodymium-isotopic compositions of Martian meteorites. Meteorit. Planet. Sci. 34 (3), 439–449. https://doi.org/10.1111/j.1945-5100.1999.tb01352.x.

Oskierski, H.C., Bailey, J.G., Kennedy, E.M., Jacobsen, G., Ashley, P.M., Dlugogorski, B. Z., 2013a. Formation of weathering-derived magnesite deposits in the New England Orogen, New South Wales, Australia: implications from mineralogy, geochemistry and genesis of the Attunga magnesite deposit. Mineral. Deposita 48 (4), 525–541. https://doi.org/10.1007/s00126-012-0440-5.

Oskierski, H.C., Dlugogorski, B.Z., Jacobsen, G., 2013b. Sequestration of atmospheric CO2 in a weathering-derived, serpentinite-hosted magnesite deposit: 14C tracing of carbon sources and age constraints for a refined genetic model. Geochim. Cosmochim. Acta 122, 226–246. https://doi.org/10.1016/j.gca.2013.08.029.

Oskierski, H.C., Beinlich, A., Mavromatis, V., Altarawneh, M., Dlugogorski, B.Z., 2019. Mg isotope fractionation during continental weathering and low temperature carbonation of ultramafic rocks. Geochim. Cosmochim. Acta 262, 60–77. https://doi.org/10.1016/j.gca.2019.07.019.

Pédrot, M., Dia, A., Davranche, M., Gruau, G., 2015. Upper soil horizons control the rare earth element patterns in shallow groundwater. Geoderma 239–240, 84–96. https://doi.org/10.1016/j.geoderma.2014.09.023.

Pope, G.J., 2007. Mineral Development Licence 196 Boundary Flat Lagoons oil Shale Project Annual Report to QDME for the Period (R 3186; Queensland Energy Resources Limited). Queensland Department of Mines and Energy.

Pourmand, A., Dauphas, N., Ireland, T.J., 2012. A novel extraction chromatography and MC-ICP-MS technique for rapid analysis of REE, Sc and Y: revising CI-chondrite and Post-Archean Australian Shale (PAAS) abundances. Chem. Geol. 291, 38–54. https://doi.org/10.1016/j.chemgeo.2011.08.011.

Power, I.M., Wilson, S., Thom, J.M., Dipple, G.M., Gabites, J.E., Southam, G., 2009. The hydromagnesite playas of Atlin, British Columbia, Canada: a biogeochemical model for CO2 sequestration. Chem. Geol. 260 (3–4), 286–300. https://doi.org/10.1016/j.chemgeo.2009.01.012.

Ratié, G., Zhang, K., Iqbal, M., Vantelon, D., Mahé, F., Rivard, C., Komárek, M., Bouhnik-Le Coz, M., Dia, A., Hanna, K., Davranche, M., Marsac, R., 2023. Driving forces of Ce (III) oxidation to Ce(IV) onto goethite. Chem. Geol. 633, 121547. https://doi.org/10.1016/j.chemgeo.2023.121547.

Raudsepp, M.J., Wilson, S., Zeyen, N., Arizaleta, M.L., Power, I.M., 2024. Magnesite everywhere: formation of carbonates in the alkaline lakes and playas of the Cariboo Plateau, British Columbia, Canada. Chem. Geol. 648, 121951. https://doi.org/10.1016/j.chemgeo.2024.121951.

Rielli, A., Boschi, C., Dini, A., 2022. Tectonically driven carbonation of serpentinite by mantle CO2: genesis of the Castiglioncello magnesite deposit in the Ligurian ophiolite of Central Tuscany (Italy). Ore Geol. Rev. 149, 105022. https://doi.org/10.1016/j.oregeorev.2022.105022.

Roelandts, I., Duchesne, J.C., 1994. 1993 compilation of data on five Belgian sedimentary rock reference materials: AWI-1, SBO-1, PRI-1, CCH-1 and DWA-1. Geostand. Newslett. 18 (2), 143–184. https://doi.org/10.1111/j.1751-908X.1994.tb00515.x.

Russell, M.J., Ingham, J.K., Zedef, V., Maktav, D., Sunar, F., Hall, A.J., Fallick, A.E., 1999. Search for signs of ancient life on Mars: expectations from hydromagnesite microbialites, Salda Lake, Turkey. J. Geol. Soc. 156 (5), 869–888. https://doi.org/10.1144/gsjgs.156.5.0869.

Ryan, C.G., 2001. Developments in dynamic analysis for quantitative PIXE true elemental imaging. Nucl. Instrum. Methods Phys. Res., Sect. B 181 (1–4), 170–179. https://doi.org/10.1016/S0168-583X(01)00374-3.

Ryan, C.G., Laird, J.S., Fisher, L.A., Kirkham, R., Moorhead, G.F., 2015. Improved dynamic analysis method for quantitative PIXE and SXRF element imaging of complex materials. Nucl. Instrum. Methods Phys. Res., Sect. B 363, 42–47. https://doi.org/10.1016/j.nimb.2015.08.021.

Scheller, E.L., Swindle, C., Grotzinger, J., Barnhart, H., Bhattacharjee, S., Ehlmann, B.L., Farley, K., Fischer, W.W., Greenberger, R., Ingalls, M., Martin, P.E., Osorio-Rodriguez, D., Smith, B.P., 2021. Formation of magnesium carbonates on Earth and implications for Mars. J. Geophys. Res. Planets 126 (7). https://doi.org/10.1029/2021JE006828.

Scheller, E.L., Razzell Hollis, J., Cardarelli, E.L., Steele, A., Beegle, L.W., Bhartia, R., Conrad, P., Uckert, K., Sharma, S., Ehlmann, B.L., Abbey, W.J., Asher, S.A., Benison, K.C., Berger, E.L., Beyssac, O., Bleefeld, B.L., Bosak, T., Brown, A.J., Burton, A.S., Zorzano, M.-P., 2022. Aqueous alteration processes in Jezero crater, Mars—implications for organic geochemistry. Science 378 (6624), 1105–1110. https://doi.org/10.1126/science.abo5204.

Searston, S., 1998. Resource Estimation and the Kunwarara Magnesite Deposit [Masters Thesis]. University of Tasmania.

Shkol'nik, S.I., Barash, I.G., Belichenko, V.G., Letnikova, E.F., 2011. Geochemistry of highly aluminiferous Vendian-Cambrian sediments of the Tunka Bald Mountains, East Sayan. Dokl. Earth Sci. 436 (1), 108–112. https://doi.org/10.1134/S1028334X11010193.

Srivastava, A.K., Bansod, M.N., Singh, A., Sharma, N., 2019. Geochemistry of paleosols and calcretes from Quaternary sediments of Purna alluvial basin, Central India: an emphasis on paleoclimate. Rhizosphere 11, 100162. https://doi.org/10.1016/j.rhisph.2019.100162.

Stack, K.M., Ives, L.R.W., Gupta, S., Lamb, M.P., Tebolt, M., Caravaca, G., Grotzinger, J. P., Russell, P., Shuster, D.L., Williams, A.J., Amundsen, H., Alwmark, S., Annex, A. M., Barnes, R., Bell, J., Beyssac, O., Bosak, T., Crumpler, L.S., Dehouck, E., Wiens, R. C., 2024. Sedimentology and stratigraphy of the Shenandoah Formation, Western Fan, Jezero Crater, Mars. J. Geophys. Res. Planets 129 (2), e2023JE008187. https://doi.org/10.1029/2023JE008187.

State of Queensland Department of Natural Resources and Mines, 2012. Queensland Geology and Structural Framework GIS Data Geology Map 2012 [Map]. State of Queensland Department of Natural Resources and Mines. https://geoscience.data.qld.gov.au/data/map-collection/mr010691.

Sun, V.Z., Hand, K.P., Stack, K.M., Farley, K.A., Simon, J.I., Newman, C., Sharma, S., Liu, Y., Wiens, R.C., Williams, A.J., Tosca, N., Alwmark, S., Beyssac, O., Brown, A., Calef, F., Cardarelli, E.L., Clavé, E., Cohen, B., Corpolongo, A., Wogsland, B., 2023. Overview and results from the Mars 2020 Perseverance Rover's first science campaign on the Jezero Crater Floor. J. Geophys. Res. Planets 128 (6), e2022JE007613. https://doi.org/10.1029/2022JE007613.

Sverjensky, D.A., 1984. Europium redox equilibria in aqueous solution. Earth Planet. Sci. Lett. 67 (1), 70–78. https://doi.org/10.1016/0012-821X(84)90039-6.

Swindle, C.R., 2023. Fluid-Rock Interactions from the Lithosphere to Earth's Surface (Version Final). California Institute of Technology. https://doi.org/10.7907/5MBH-JW64. PDF.

Swindle, C., Vasconcelos, P., Dalleska, N., Cardarelli, E., Bhattacharjee, S., Dimarco, Z., Farley, K.A., Present, T., 2025. Trace element compositions and redox shifts preserved in magnesites, sediments and soils from the Kunwarara magnesite mine. Appl. Geochem., 106494 https://doi.org/10.1016/j.apgeochem.2025.106494.

Ternieten, L., Früh-Green, G.L., Bernasconi, S.M., 2021. Distribution and sources of carbon in serpentinized mantle peridotites at the Atlantis Massif (IODP expedition 357). J. Geophys. Res. Solid Earth 126 (10), e2021JB021973. https://doi.org/10.1029/2021JB021973.

Thompson, A., Amistadi, M.K., Chadwick, O.A., Chorover, J., 2013. Fractionation of yttrium and holmium during basaltic soil weathering. Geochim. Cosmochim. Acta 119, 18–30. https://doi.org/10.1016/j.gca.2013.06.003.

Tutolo, B.M., Hausrath, E.M., Kite, E.S., Rampe, E.B., Bristow, T.F., Downs, R.T., Treiman, A., Peretyazhko, T.S., Thorpe, M.T., Grotzinger, J.P., Roberts, A.L., Archer, P.D., Des Marais, D.J., Blake, D.F., Vaniman, D.T., Morrison, S.M., Chipera, S., Hazen, R.M., Morris, R.V., Vasavada, A.R., 2025. Carbonates identified by the Curiosity rover indicate a carbon cycle operated on ancient Mars. Science 388 (6744), 292–297. https://doi.org/10.1126/science.ado9966.

Uno, M., Koyanagawa, K., Kasahara, H., Okamoto, A., Tsuchiya, N., 2022. Volatile-consuming reactions fracture rocks and self-accelerate fluid flow in the lithosphere. Proc. Natl. Acad. Sci. 119 (3), e2110776118. https://doi.org/10.1073/pnas.2110776118.

Vaniman, D.T., Whelan, J.F., 1994. Inferences of Paleoenvironment from Petrographic, Chemical and Stable-Isotope Studies of Calcretes and Fracture Calcites, p. 9. http://inis.iaea.org/search/search.aspx?orig_q=RN:25070370.

Warren, J.K., 1990. Sedimentology and mineralogy of dolomitic Coorong Lakes, South Australia. SEPM J. Sediment. Res. 60. https://doi.org/10.1306/212F929B-2B24-11D7-8648000102C1865D.

Wilcock, S., 2000. Kunwrara Magnesite Deposit, pp. 129–133.

Yusheng, W., Jianxin, Z., Jingsui, Y., Zhiqin, X., 2006. Geochemistry of high-grade metamorphic rocks of the North Qaidam mountains and their geological significance. J. Asian Earth Sci. 28 (2–3), 174–184. https://doi.org/10.1016/j.jseaes.2005.09.018.

Zeissink, H.E., 1969. The mineralogy and geochemistry of a nickeliferous laterite profile (Greenvale, Queensland, Australia). Mineral. Deposita 4, 132–152.

Zhang, K., Shields, G.A., 2022. Sedimentary Ce anomalies: secular change and implications for paleoenvironmental evolution. Earth Sci. Rev. 229, 104015. https://doi.org/10.1016/j.earscirev.2022.104015.